Simulation of Rutherford backscattering spectrometry from arbitrary atom structures

S. Zhang (张硕)[*]

School of Nuclear Science and Technology, Lanzhou University, Lanzhou, Gansu Province 730000, People's Republic of China
and Department of Physics, University of Helsinki, P.O. Box 43, FIN-00014 Helsinki, Finland

K. Nordlund and F. Djurabekova

Department of Physics and Helsinki Institute of Physics, University of Helsinki, P.O. Box 43, FIN-00014 Helsinki, Finland
and National Research Nuclear University MEPhI, Kashirskoye sh. 31, 115409 Moscow, Russia

Y. Zhang and G. Velisa

Materials Science and Technology Division, Oak Ridge National Laboratory, Oak Ridge, Tennessee 37831, USA

T. S. Wang

School of Nuclear Science and Technology, Lanzhou University, Lanzhou, Gansu Province 730000, People's Republic of China

Rutherford backscattering spectrometry in a channeling direction (RBS/C) is a powerful tool for analysis of the fraction of atoms displaced from their lattice positions. However, it is in many cases not straightforward to analyze what is the actual defect structure underlying the RBS/C signal. To reveal insights of RBS/C signals from arbitrarily complex defective atomic structures, we develop here a method for simulating the RBS/C spectrum from a set of arbitrary read-in atom coordinates (obtained, e.g., from molecular dynamics simulations). We apply the developed method to simulate the RBS/C signals from Ni crystal structures containing randomly displaced atoms, Frenkel point defects, and extended defects, respectively. The RBS/C simulations show that, even for the same number of atoms in defects, the RBS/C signal is much stronger for the extended defects. Comparison with experimental results shows that the disorder profile obtained from RBS/C signals in ion-irradiated Ni is due to a small fraction of extended defects rather than a large number of individual random atoms.

I. INTRODUCTION

As a conventional ion beam analysis (IBA) method, Rutherford backscattering spectrometry (RBS) has been widely used to investigate the structure and composition of materials by measuring backscattering yields and energy spectra of swift light ions (typically α ions) from a sample of interest. If the probe ions are impinging on the surface in a channeling condition, the method is known as RBS/C (or RBS in a channeling direction). In the RBS/C technique, backscattering yields increase due to imperfections in crystals. These yields are then used to analyze the fraction of defective atoms in crystals. The technique has been widely used to characterize the damage of crystalline materials produced by, e.g., ion irradiation [1–3].

Quantitative analysis of RBS/C signals, however, is fairly confounded as extended defects formed due to point-defect agglomeration may affect the signal of backscattered ions. The extent of this uncertainty can be estimated via a direct simulation of RBS/C spectra from structures obtained by atomistic simulation of the irradiation process under conditions of interest.

In the past decades, several methods were developed to simulate or calculate the RBS/C spectra from a crystal containing defects. Among these methods, the two-beam methods [4–6], a name used for all methods that distinguished the probe beam as channeling and dechanneling fractions,

were commonly used in the analysis of RBS/C results. In these methods, the backscattered ions from the interaction of channeling ions with defect atoms and those from the interaction of dechanneled ions with atoms are calculated separately. A typical implementation of these methods is the *iterative procedure* [5,7–9], where three spectra are required: a RBS/C spectrum from a sample that is to be analyzed, a spectrum from a pristine sample (perfect crystal), and a nonchanneling RBS spectrum. The dechanneling component, assumed to be zero, starts from a channel on the pristine spectrum either right after the surface peak (when the damage is close to the surface) or near the beginning of the damaged region, and may stop at a channel beyond the damage region where the dechanneling component overlaps with the RBS/C spectrum. The iterative procedure successively moves in depth to the next channel to determine the dechanneling contribution and to identify the displaced atoms at that depth. This method can be used to extract a depth profile of disorder in the damaged crystal sample. The disorder here, in general, refers to all types of imperfections in crystals, including point defects, extended defects, distortions, amorphization, etc. Another widely used method is based on a Monte Carlo approach [10–14]. The first successful Monte Carlo simulation of the RBS/C spectra from crystals was developed by Barrett [10] in 1971. After this pioneering work, several Monte Carlo codes for RBS/C simulations were developed by different groups. One of them, the code FLUX [11], combines the binary collision and the multistring approximations and can be used to simulate backscattering yields of probe ions passing through the crystals. This code is usually only used for pristine crystals.

---
[*]Corresponding author: shzhang15@gmail.com

The Monte Carlo Channeling SYmulation (MCCHASY) code [12] developed by Nowicki *et al.* uses the binary collision model and nuclear encounter probability approach to simulate the RBS/C spectra from crystals containing defects. It has been successfully used to analyze the fraction of displaced atoms in monoelemental, multielemental, and multilayered crystals [15]. Moreover, the randomly displaced atoms (RDAs) and long-range extended defects, such as dislocations, can be distinguished in MCCHASY [16]. However, the MCCHASY code lacks the ability to analyze structural defects, such as distortion around defects and the corresponding strain fields, i.e., the real atomic structure around a defect cluster. Another Monte Carlo code, BISIC [13,14], was developed based on the binary collision approximation (BCA) code MARLOWE [17]. Instead of simply regarding the defect as RDAs, BISIC takes the real atomic structure into account. It has been used to simulate the RBS/C signals from structures with point defects, taking the distortion caused by interstitials and vacancies into account [18,19].

All the methods mentioned above are able to calculate or simulate the RBS/C spectra from crystals with some simple defects. Moreover, some methods, like the iterative procedure, MCCHASY, and BISIC, have been very successfully used to analyze the fraction of defective atoms in the damaged crystalline materials. None of the existing codes, however, is able to simulate the RBS/C signals from an arbitrary atomic structure. Hence the existing codes are not able to reveal the effect of extended defects on RBS/C signals. This indicates a need for a specific type of code to deal with complex arbitrary structures containing different types of defects or heavily damaged structures. Such a code will improve the interpretation of the RBS/C results and enhance the usage of this versatile and nondestructive analysis technique. Moreover, it will provide insights of structural defects for more quantitative analysis.

In this paper, we introduce a BCA-based code RBSADEC (RBS-C of Arbitrary Defected Crystals) to simulate the RBS spectrum from a crystal structure with arbitrarily assumed defects in it. The read-in atom coordinates for the RBSADEC code can be obtained from separately performed molecular dynamics (MD) simulations. In the current work, we use the MD method to create an arbitrary structure with controllably introduced defects of different types.

This paper is organized as follows. The experiments which were used to compare the simulation results are described in Sec. II. The RBSADEC algorithm and how the read-in atom structures were created by using the MD method are presented in Sec. III. In Sec. IV the simulation results as well as the comparison of the simulation and experimental results are presented and discussed. Section V contains the summary.

II. EXPERIMENTS

Experiments on ion radiation were carried out at room temperature in a pure Ni sample which is irradiated by 1.5 MeV Mn^+ to a fluence of 6.4×10^{13} cm^{-2}. After irradiation, the sample was analyzed using the standard RBS/C technique to determine the irradiation damage. The experiment was performed in the Ion Beam Materials Laboratory (IBML) [20], University of Tennessee. The analyzing beam (α ions) impinged along the $\langle 100 \rangle$ crystalline axis into the samples

and the energy of the beam was 3.5 MeV. An energy-resolved silicon detector was placed in the backscattering angle of 155° with the impinging direction to measure the energy spectra of the backscattered ions.

III. SIMULATION METHODS

A. Approach to simulate RBS/C spectrum from read-in atom coordinates

The BCA technique is a method to simulate the process of ion irradiation of materials. In this method, the ions impinging on the surface scatter by subsequent individual ion-atom collision events ("nuclear stopping power") and slow down mainly due to inelastic interactions with target electrons ("electronic stopping power"). Between two successive collisions, the movement of ions is usually regarded to occur along a straight path. The BCA method has been proven to describe successfully irradiation of either crystalline or amorphous materials, by energetic ions with relatively high energies ($> \sim$ several keV/amu).

In the present work, the conventional BCA method was applied to simulate the three-dimensional paths of energetic ions inside of a material. Unlike the existing BCA codes, where the material structure is either assumed amorphous [21–23] or simulated by using a translational symmetry of crystals [17,24], our code RBSADEC reads in three-dimensional atom coordinates of an arbitrary structure in a standard *XYZ* file format widely used in computational chemistry. The arbitrary structures can be produced by, e.g., MD simulations and confirmed experimentally by microstructure analysis [25–27]. Hence, the structures can contain different types of defects naturally distributed in the structure.

Figure 1 illustrates the implemented simulation method. Here, the positions of atoms (solid circles) are read in from the input file. The atoms displaced from their lattice positions represent the defects as described by atom coordinates from a read-in file. The solid lines show a path of an incident ion (the open circle). In principle, the RBS/C spectrum can be directly obtained by collecting the backscattered probe ions at the detector placed at a certain angle with respect to the surface of the investigated sample.

The very low Rutherford backscattering cross sections introduce additional ambiguity in analysis of the spectra of backscattered ions due to poor statistics. To deal with
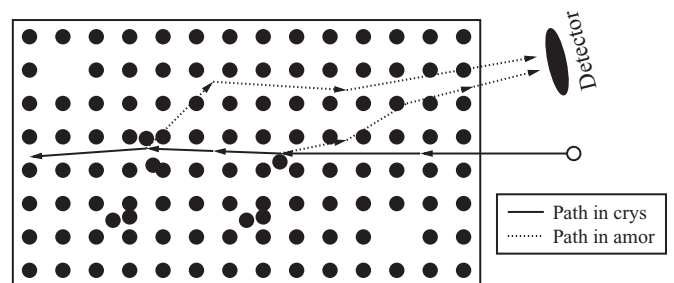

FIG. 1. The schematic diagram of the RBS/C simulation. The solid line shows the path of a real ion, while the dashed lines show the paths of virtual ions used to speed up the RBS data collections (see text).

this problem, we use a so-called *encounter probability* [10] (see Sec. III A 4), which is the normalized probability of an incident ion to be backscattered in every ion-atom collision. This probability is used to generate a virtual (weighted) backscattered ion. A virtual ion represents distribution of the Rutherford backscattering probabilities of the probe ion on an encountered target atom. It is necessary to take into account the distribution of the probabilities instead of a single value, since the target atom is not still but moving around its equilibrium position due to thermal vibrations. We consider this backscattering probability as a weighted object—an ion— with all the corresponding properties of an incident ion, but its contribution to the final backscattering yield is weighted according to the Rutherford backscattering probability at the current place. This virtual ion does not interact with the real ion in any way and is only used to account for the probability of Rutherford backscattering on a colliding target atom. The virtual ion moves along the backscattered direction, while the real ion continues its motion (solid line in the figure) in the structure.

The paths of the virtual backscattered ions are indicated by dashed lines in Fig. 1, which are terminated inside the material or leave the surface. Since the virtual backscattered ions are not in the channeling regime anymore, for computational efficiency they are traced back to the surface according to the amorphous structure BCA algorithm as in Refs. [22,28].

After a virtual backscattered event, those virtual ions which were emitted from the surface in the direction of the detector are collected for the calculation of RBS spectra. The trajectories of real ions are used to calculate the range of incident ions.

The RBSADEC can simulate the ranges of various ions in single- and multielement samples but not in the multilayered samples. Similarly, for RBS/C simulations, the probe ions can be various light ions (e.g., H^+, D^+, or α particles), while the samples have to be single layered. In principle, this code works well in the energy region where the BCA algorithm is valid (roughly from 100 eV to 1 GeV). But for RBS/C simulations, the energies of probe ions had better be larger than ~100 keV.

Since RBSADEC utilizes the BCA algorithm, this code is far more efficient and inexpensive than MD simulations. The code can be easily run on ordinary personal desktop with dual-core (or more) CPUs and 2 gigabyte (or larger) memory. The RBS/C simulations usually take from a few minutes to hours, depending on the system simulated.

In the following we discuss the algorithm in more detail.

1. How to find an atom for a collision in BCA

The atomic structure that contains defects and is to be analyzed by the RBS/C technique is referred as the "structure" in the text, and an incident ion (α particle) as a projectile.

The approach of finding an atom—a partner for collision (or simply a partner)—that is used in RBSADEC is shown in Fig. 2. All atoms in the structure that are located in front of the moving projectile P (the projections of the vectors connecting P and the atoms on the projectile direction $\vec{\lambda_0}$ are positive) are denoted as T_i ($i = 1, 2, \ldots$). The impact parameters p_i ($i = 1, 2, \ldots$) of all atoms T_i are calculated and compared to the maximum impact parameter R_{max}, which is defined as
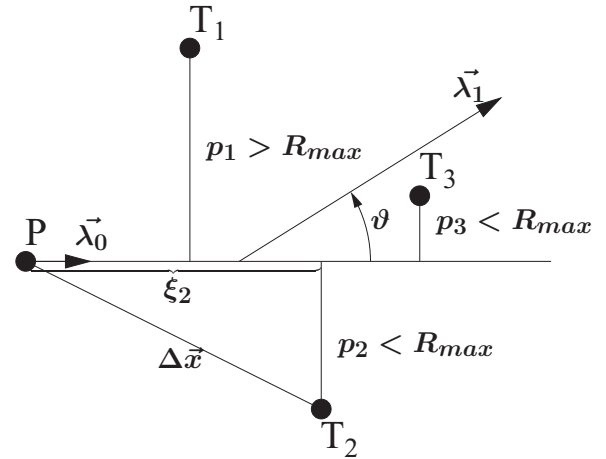

FIG. 2. Illustration of how a collision partner is found in RBSADEC.

$R_{max} = n^{-\frac{1}{3}}$, where n is the atomic density of the structure. The closest atom T_i along $\vec{\lambda_0}$ with the impact parameter $p_i < R_{max}$ is selected to be a partner. For instance, in Fig. 2, the atom T_2 is selected to be the partner since it is the closest atom in the illustrated example with the impact parameter less than R_{max} in the direction $\vec{\lambda_0}$.

After the collision, a partner is sought along a new direction $\vec{\lambda_1}$, resulting from the previous collision. In the new search, the atom that experienced the collision in the previous step is excluded to avoid multiple collisions with the same atoms. Thus, in the example of Fig. 2, the atom T_2 will be excluded from the list of possible partners along the direction $\vec{\lambda_1}$.

To collect statistically significant information for accurate RBS/C analysis of the structure, it is necessary to simulate rather large structures with big numbers of atoms. Searching for a partner among all the atoms of the structure becomes computationally inefficient, since it requires computing the impact parameters of every atom. In RBSADEC, we utilized the same linked-cell algorithm [29] as implemented in the PARCAS MD code [30,31]. This algorithm allows for searching for a partner only within the closest proximity of the current position of the projectile.

In the linked-cell algorithm, the simulation box is first divided into small cells of a size slightly larger than the maximum impact parameter R_{max}. The cell currently hosting the projectile is labeled C_p. The partner is sought in the cell C_p or in the cells immediately neighboring C_p. Then, a partner is found based on calculation of the impact parameters of the atoms inside the C_p and surrounding cells (for three-dimensional simulations, a total of 27 cells) instead of in the entire structure. If all the calculated impact parameters are larger than R_{max}, i.e., the partner is not found, the projectile will move a straight distance the size of the cell in the original direction, after which the procedure of finding a collision partner is repeated again.

2. Basic binary collision approximation

In our RBSADEC code, the scattering event is calculated according to the BCA algorithm. Scattering angles and the time integral of a binary collision for different impact parameters
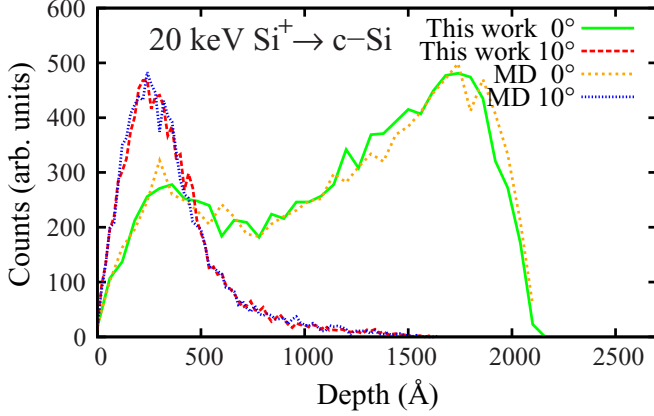
FIG. 3. The depth profiles of 20-keV Si ions in c-Si with different incident angles simulated by the present RBSADEC code and the MDRANGE code.

FIG. 4. The depth profiles of He ions in amorphous silicon with different energies simulated by RBSADEC and TRIM.

and initial energies are precalculated within the universal Ziegler-Biersack-Littmark (ZBL) screened interatomic potential [32] by using the Gauss-Mehler quadrature integration method [33]. These values are tabulated and used on demand to find the new direction $\vec{\lambda}_1$ and position of the scattered projectile. More details on the approach realized in the current algorithm can be found in Ref. [17].

The energy loss for electronic excitation in terms of electronic stopping power, which is from the Stopping and Range of Ions in Matter (SRIM) database [23], is subtracted between the collisions from the energy of the moving projectile. In the RBS/C technique, the irradiation of probe ions (α particle) does not and should not lead to significant changes of the structures of the studied samples. Therefore, in our simulation, the motion of knocked-on atoms are not followed; i.e., the read-in atomic structure is not updated during the simulation.

3. Comparison of ion range profiles by BCA and MD approaches

The simulation of the ion path in the material is crucial for the RBS/C simulation. This is why it is important to verify the results obtained from the current code against the results obtained from an MD approach. We compare the ion range distributions in crystals obtained by the RBSADEC and the MDRANGE [34,35] codes. In the latter code, the path of an ion, producing primary knocked-on atoms only, is followed using the molecular dynamics algorithm. The MDRANGE code has previously been tested against a wide range of experimental data [35–41]. Figure 3 shows an excellent agreement of the ion range profiles obtained in crystalline silicon (c-Si) by both RBSADEC and MDRANGE for 20-keV Si ions with two incident angles $0°$ (along the channeling direction) and $10°$ off the $\langle 001 \rangle$ crystallographic direction of the Si crystal.

A long "channeling tail" of the Si ion range profiles is clearly seen for both results for the normal incident angle of ions (in the channeling condition). With a tilt of the incident angle ($10°$ off the normal), the "channeling tail" disappears. Additionally, we simulated the range profiles of other ion-target combinations, such as He on W, Ni on c-Si, as well as Xe on Au. All comparisons showed good agreement within the statistical uncertainty.
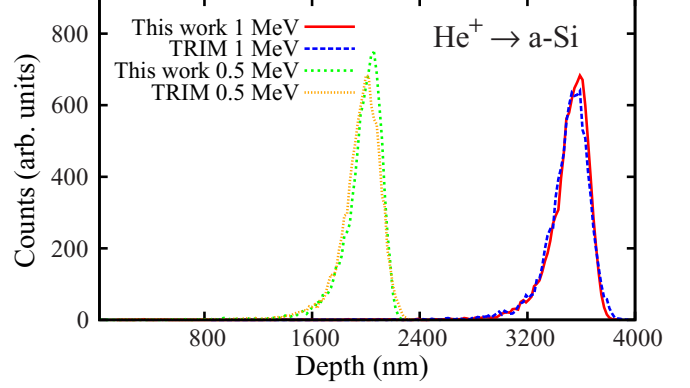
Since we aim to analyze the structure containing arbitrary defects, we also compare the results of our code with the Transport of Ions in Matter (TRIM) [23] ion range calculations. Hence we created a random structure with a given atomic density, which can be interpreted as an amorphous sample. Then the ion ranges simulated in this structure were compared with the results obtained by TRIM for the same materials. Thus, Fig. 4 illustrates the perfect agreement obtained for the He ion depth profiles in amorphous silicon simulated by both codes.

In addition, Table I lists the ranges of He in silicon and Ni with different energies. All the results show very good agreement.

4. Virtual backscattered ions

In the current algorithm, we consider the encounter probability that describes the probability of an ion-atom collision with a very small impact parameter. In these collisions, either the ion is reflected or a nuclear reaction occurs. Let us assume that x and y are orthogonal axes that are perpendicular to the direction of ion motion. Then, in one collision, the encounter probability Q_i normalized by random collision can be expressed by the formula

$$Q_i = \frac{1}{2\pi\mu_a^2}\exp\left(\frac{(x_i - x_a)^2 + (y_i - y_a)^2}{-2.0\mu_a^2}\right), \qquad (1)$$

TABLE I. The ranges of He ions in Si and Ni.

Materials	Incident energy (keV)	Mean ranges (nm)	
		Present work	TRIM
Si	20	202.4 ± 2.2	204.1 ± 2.2
	100	675.2 ± 3.9	672.3 ± 4.1
	200	1062.0 ± 4.4	1050.7 ± 4.4
	500	1975.1 ± 4.9	1963.0 ± 4.9
	1000	3502.5 ± 5.5	3505.7 ± 5.2
Ni	20	75.3 ± 1.2	77.2 ± 1.1
	100	289.4 ± 2.7	288.8 ± 2.6
	200	495.0 ± 3.2	487.8 ± 3.3
	500	961.8 ± 4.2	969.0 ± 3.9
	1000	1676.9 ± 4.1	1680.2 ± 4.3

where $x_{i,a}$ and $y_{i,a}$ are the coordinates of the ion and the atom participating in the collision; μ_a is the one-dimensional standard deviation of thermal vibrations which can be obtained from the Debye theory [42].

The backscattering yield from one collision Z_i can be obtained by collecting virtual ions, i.e., probabilities that a projectile will be backscattered and thus have an opportunity to reach the detector. If the trajectories of backscattered ions are exactly straight lines, this collection of virtual ions can be expressed by the integration

$$Z_i = \int_0^{\Delta\Omega_d} Q_i \sigma(\theta) d\Omega, \qquad (2)$$

where $\Delta\Omega_d$ is the solid angle of the detector, θ is the backscattering angle, and σ is the Rutherford cross section. In this RBS/C simulation, Q_i is the probability to generate a virtual backscattered ion and $\sigma(\theta)$ defines the weight (ω) of the generated virtual ions. As it is seen in Eq. (1), the probability Q_i may be larger than unity. This means that more than one virtual ion can be generated in a single collision.

Based on the Monte Carlo algorithms, the Eq. (2) is expressed as

$$Z_i = \frac{\sum\limits_{t=1}^{N_1} Q_i \sigma(\theta_t)}{N_1} \Delta\Omega_d, \qquad (3)$$

where θ_t is a backscattered angle (initial directions of virtual ions) randomly chosen inside of the solid angle $\Delta\Omega_d$. The total backscattering yield Y is the summation of the yield from every single collision Z_i,

$$Y = \sum_{i=1}^{N_2} Z_i, \qquad (4)$$

where i is the index of collisions and N_2 is the number of collision events simulated. In our simulation N_2 is sufficiently large to fulfill the requirement of good statistics; thus we chose N_1 [in Eq. (3)] equal to 1, i.e., the initial directions of virtual ions are randomly chosen inside of solid angle $\Delta\Omega_d$ in all collision events.

In reality, a virtual ion which has an initial direction inside (or out) of the solid angle $\Delta\Omega_d$ still might not (or might) result in a signal on the detector due to the multiple scattering on the way back to the surface. To produce RBS/C spectra including this multiple scattering effect in an efficient way, it is very important to optimize the choice of initial directions of virtual ions. This issue has been addressed in Ref. [43], where the initial directions of scattered ions were refined to a solid angle $\Delta\Omega_c$, which is larger than that of the detector $\Delta\Omega_d$ and encloses up to 95% of scattered ions. This approach was used later in Ref. [21]. In the current simulations, we refined the initial direction of virtual ions to the solid angle $\Delta\Omega_c = \pi$, which has an opening angle $\theta_c = 120°$ and a symmetric axis from the place where the collision took place towards the center of the detector. This solid angle $\Delta\Omega_c$ is enough to include almost all of the possible initial directions that can make virtual ions finally contribute to an RBS/C signal due to multiple scattering, since the energies of probe ions in the RBS/C technique are usually of MeV energy range. In this range the

multiple scattering effect does not change the initial direction dramatically. This way, we reduce the computational time spent on the trajectories of virtual ions which do eventually not reach the detector.

5. Simulation of RBS/C signals

When the virtual backscattered ion j reaches the detector, the energy E_j, which corresponds to a channel number H_j and a weight (ω_j) of the ions, is used to calculate the spectrum. To take the energy straggling introduced by the detector into account, the energy of detected ions spreads in a Gaussian shape. The spectrum is calculated as follows [21]:

$$C[i] = \frac{1}{\sqrt{2\pi}\sigma_d} \sum_j^N \omega_j \exp\left(\frac{(H_i - H_j)^2}{-2\sigma_d^2}\right), \qquad (5)$$

where $C[i]$ are the counts in channel i, j is the index of detected ions, N is the total number of detected ions, ω_j is the weight of the jth detected ions, σ_d is the resolution of the detector divided by energy interval, H_i is the channel number i, H_j is the channel number which corresponds to the energy of the jth detected ions. The yield of RBS-C can be expressed by the formula

$$Y[i] = \frac{C[i]}{N_h} \Delta\Omega_c, \qquad (6)$$

where $Y[i]$ is the yield in channel i, N_h is the number of simulated incident ions, and $\Delta\Omega_c$ is the solid angle of the cone which the emitted direction of backscattered ions are confined into.

B. Methods to create defective crystal structures

The MD method is widely used to study macroscopic and microscopic properties of materials. MD simulations have proven to be able to predict reasonably well final atomic structures that are damaged by, e.g., ions, photons, and so on [44,45]. Hence we chose to employ the MD method to relax the structure, after some defects were introduced by removing or adding atoms into this structure. The relaxed defective structures include a reasonable description of the lattice distortion (strain) caused by the defective atoms.

To distinguish the difference between RBS/C signals generated due to the different defects, three types of defects, including RDAs, Frenkel point defects, and extended defects, were respectively introduced into the crystalline Ni structures by different techniques in this work. The structures containing point defects or extended defects were relaxed by MD methods to mimic the distortion around defects, while the one containing RDAs without relaxation was used to reveal the effect of the distortion on the RBS/C signals.

In the RBS/C technique, the paths of the probe ions are almost straight lines along the impact direction due to the high energy of ions and a small mass. In addition, the fraction of defective atoms usually varies with the depth of the sample. To comply with these conditions, we used a simulation box with a size of $30 \times 30 \times 3600$ lattice units. The long side of the box was chosen along the [001] crystallographic direction to coincide with the z coordinate. This direction was also used to analyze the defective structure of the sample as a function
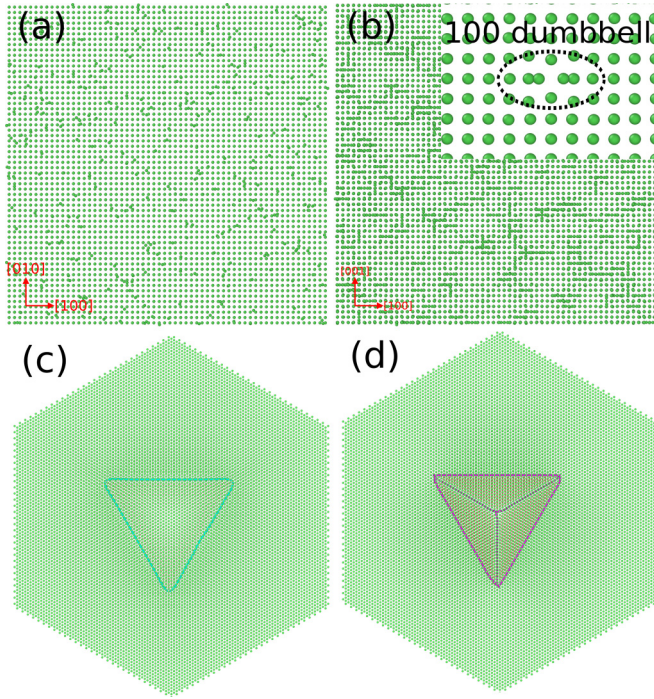
FIG. 5. The atomic structures with (a) 0.3 at.% randomly displaced atoms from the ⟨001⟩ view, (b) 0.3 at.% interstitials plus vacancies from the ⟨001⟩ view, with the inset showing the close view of ⟨100⟩ dumbbell, (c) 0.3 at.% interstitials forming extrinsic SF from the ⟨111⟩ view, and (d) 0.3 at.% vacancies forming a stacking fault tetrahedron from the ⟨111⟩ view.

of depth. Periodic boundary conditions are used in the other two directions, i.e., x and y.

To create the atomic structure that contains defects, first, we built pristine face-centered cubic (fcc) crystalline Ni cells with the equilibrium lattice constant ($a = 3.5196$ Å). Then, different types of defects were introduced into the created crystalline cells applying the corresponding techniques described below. One type of defect was created at a time.

1. Randomly displaced atoms

In our simulations, RDAs are the defects formed by randomly displaced lattice atoms without stress relaxation of the stress caused by these displacements. Even though this model of point defect is rather unphysical, it has been widely used in RBS/C simulations because the dechanneling of probe ions by this defect can be solved analytically [4]. The RBS/C yields obtained from such a structure then are compared to those obtained from the structure with point defects that was relaxed in MD simulations.

In this work, to create a RDA, a lattice atom was randomly selected and displaced. The displacement in every dimension was randomly chosen from the range $[-a/2, a/2]$, where a is the lattice constant. Figure 5(a) demonstrates an atomic structure with 0.3 at.% RDAs in a cube of size $30 \times 30 \times 30$ lattice units obtained in this manner. The image shows the defects in the ⟨100⟩ crystallographic direction (top view).

2. Point defects

Frenkel-pair-type point defects, i.e., vacancies and interstitials, were created by removing an atom from a randomly chosen lattice site or adding an extra atom between the two randomly selected neighboring lattice sites in the structure. For interstitials, to avoid the added atoms being too close to lattice atoms, the interstitials were added at one of the energetically favorable positions, i.e., the octahedral interstitial sites.

The number of vacancies (removed atoms) is the same as that of interstitials (added atoms) to ensure conservation of the total number of atoms in the simulation box. The minimum distance between the point defects was set to 10 Å to avoid spontaneous annihilation or clustering of the point defects during the MD relaxation.

The created system containing the vacancies and interstitials was relaxed by the conjugate gradient (CG) algorithm, implemented in the LAMMPS code [46]. The embedded atom method (EAM) potential [47] was used in these simulations. The analysis of the number of defects after the relaxation did not indicate any significant change in the number of defects. The demonstration of the relaxed atomic structure with point defects in the size of $30 \times 30 \times 30$ lattice units from the view of orientation ⟨100⟩ is given in Fig. 5(b). As is shown by the inset in the figure, the added self-interstitial shared a lattice position with the original lattice atom and formed a ⟨100⟩ dumbbell structure after relaxation.

3. Extended defects

Dislocations, stacking faults (SFs), and stacking fault tetrahedra (SFT) are the extended defects that are most commonly observed in metals and metal alloys irradiated by ions at room temperature. In a previous study, both experimental results and MD simulations [26] showed that the self-interstitials created by ion irradiation in Ni tend to agglomerate forming an interstitial loop, i.e., an extrinsic (or interstitial) type of stacking fault surrounded by Frank partial dislocations with Burgers vector $\frac{1}{3}\langle 111 \rangle$. The clusters of vacancies in ion-irradiated Ni may form a stacking fault tetrahedron via different formation mechanisms [48–50]. Hence here the extrinsic SFs and SFT were introduced into the simulation cells to reveal how the agglomeration of interstitials and the clustering of vacancies (extended defects) are reflected in the RBS/C signals.

To create stacking faults, one needs to pay particular attention to the stacking sequence of the atom structure. As shown in Fig. 6, the stacking sequence in a perfect fcc crystal is $\cdots$ ABCABC $\cdots$, where A, B, and C are the different {111}
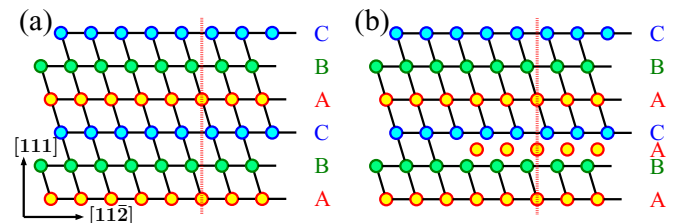

FIG. 6. Stacking sequence of (a) perfect fcc structure and (b) extrinsic stacking faults (before relaxation).

layers. Extrinsic stacking faults can be created by adding an extra {111} atom layer in perfect crystal. As shown in Fig. 6(b), the stacking sequence after adding an extra layer A becomes $\cdots$ AB | A | CABC $\cdots$, where the symbol | denotes the location of the stacking faults. The red line in Fig. 6(b) guides the eyes to the added atoms (interstitials) that were created in the exact middle of the two equivalent {111} layers, i.e., octahedral interstitial sites of the fcc structure. In the present work, we added an extra {111} atom layer with an equilateral triangular shape to the crystalline structures. Therefore, the extrinsic stacking faults were created inside of this triangular area. At the same time, a partial dislocation loop with Burgers vector of $\frac{1}{3}\langle 111 \rangle$ was formed, outlining the edge of this extra layer.

For SFT, several formation mechanisms have been confirmed by various simulations [50–52]. Among these, the most widely discussed one was proposed by Silcox and Hirsh [48], which can be briefly described as follows. First the cluster of vacancies collapses to form a Frank partial dislocation loop. The formed Frank dislocation loops then dissociate into stair-rod partial dislocations and Shockley partial dislocations. Finally, a stacking fault tetrahedron is formed by the gliding of Shockley partials towards the apex of the tetrahedron.

To create the SFT in this work, we removed one {111} atom layer with an equilateral triangular shape to imitate the initial condition of Silcox and Hirsh processes, i.e., a collapse of a cluster of vacancies. After the atoms were removed, Frank partials formed at the edge of this removed equilateral triangle. Here we only created the initial condition for Silcox and Hirsh processes. The formation of a complete stacking fault tetrahedron came out of the relaxation procedure.

Finally, the structures created by removing or adding atoms were relaxed by the same procedure as for the structure with Frenkel pair defects. During the relaxation, the SFT were formed according to the Silcox and Hirsh processes. The extrinsic stacking faults with reasonable distortion and the partial dislocations surrounding these extrinsic stacking fault atoms were created after relaxation. Figure 5 shows the $\langle 111 \rangle$ view of the atomic structure with extrinsic stacking faults in a region with size $30 \times 30 \times 30$ lattice units. The cyan line in the figure is the Frank partial dislocation loop surrounding the extrinsic stacking faults. The dislocation analysis shown in this figure was performed by the atomic structure visualization software OVITO [53]. Figure 5(d) is also the $\langle 111 \rangle$ view of the atomic structure of a stacking fault tetrahedron; the violet lines show the stair-rod dislocations that formed the stacking fault tetrahedron. In the remainder of this paper, the extended defects refer to the structure containing both extrinsic SFs and SFT.

IV. RESULTS AND DISCUSSION

A. Simulated RBS/C spectra

To reveal the sensitivity of RBS/C signals to different defects, atom structures with the same depth profiles but different types of defects were created. The depth profiles of defects were chosen in the form

$$n_D(z) = \begin{cases} 0, & z < 900 \\ 0.24 \text{ at.\%}, & 900 < z < 1800 \\ 0, & z > 1800, \end{cases} \tag{7}$$
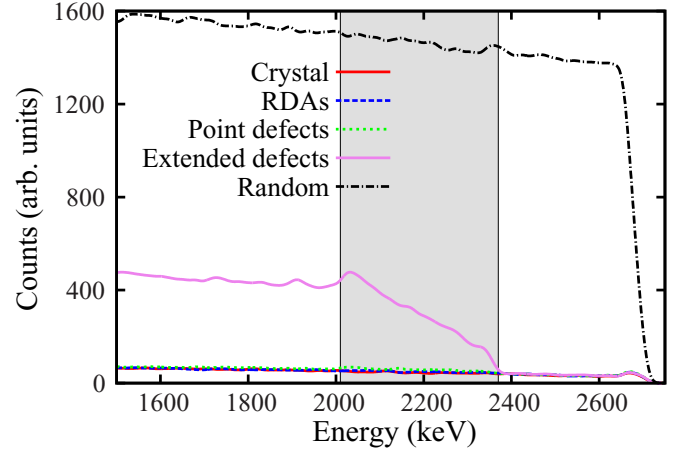

FIG. 7. Simulated RBS/C spectra from the crystal structure, from the structure with randomly displaced atoms, from the structure with Frenkel point defects, from the structure with extended defects, and from an amorphous structure. For each kind of defect, 0.24 at.% defective atoms are uniformly distributed in the middle region which is indicated by the shadowed area.

where the depth z is written in lattice units. For convenience, in the following, the region with depth $z < 900$ is referred to as the surface region, $900 < z < 1800$ as the middle region, and $z > 1800$ as the deep bulk region. The number of RDA defects was counted by the number of displaced atoms, while the interstitials (vacancies) meant added (removed) atoms. For the extended defects, the concentration of defects in the present work was also counted by the number of interstitials that formed extrinsic stacking faults, or the vacancies that formed the SFT.

After creating the atom structures with RDAs, point defects, or extended defects, we used the RBSADEC code to simulate the RBS/C spectra from these structures. All the parameters used in the RBS/C simulations, e.g., the energy of probe ions, geometry of the experimental setup, and so on, are the same as in the experiment (see Sec. II). To provide the reference level, the RBS/C spectra from a pristine crystal and a random structure were simulated as well. For all the simulations, the incident angle of the probe ions (He) was allowed to have an uncertainty of 0.1° to emulate the effect of various systematic uncertainties in the experiment, e.g., spread of angle and energy of the probe ions, imperfection in surface of pristine samples, and so on. The simulated spectra are shown in Fig. 7. Here, the red, blue, green, violet, and black lines show the RBS/C spectra of the pristine crystalline structure, the structures with RDAs, with point defects, with extended defects, and with random (amorphous) structure, respectively.

The RBS/C spectra in the energy range [2400,2750] correspond to the structures of the surface regions of the simulation boxes. Since in all studied structures the surface regions were left intact (pristine crystals), the energy spectra are almost identical to the spectrum of a crystal in this energy range.

The energy range of [2000,2400] corresponds to the depth of the defective structures in the middle region (shaded area in Fig. 7). In this region, the RBS/C yields from the structure with extended defects are significantly larger than either those from
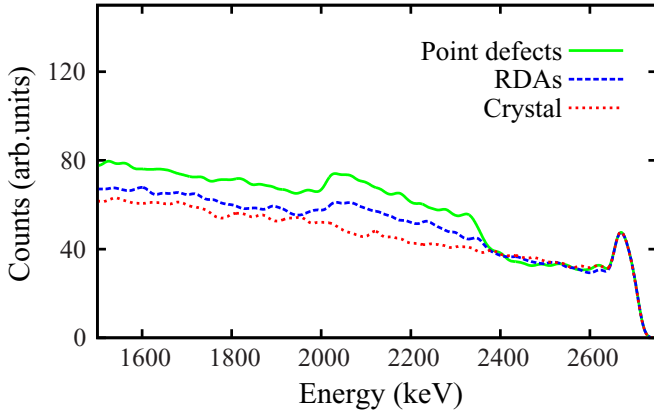
FIG. 8. Simulated RBS/C spectra from the crystal, the structure with randomly displaced atoms, and the structure with point defects. The signal is for 0.5 at.% RDAs or point defects uniformly distributed in middle region.

the structure with point defects or those from the structure with RDAs, which indicates the RBS/C signal is much more sensitive to extended defects than to point defects or RDAs. Both the structure with extended defects and the structure with point defects were relaxed by MD procedures. The main difference between the two structures is that a strong strain field exists in the structure with extended defects, but not in that with point defects. Therefore, this strain field induced by extended defects might be the cause of the significant difference in RBS yields obtained from the two structures.

The middle region contains different structural defects and the RBS/C spectra from this region are expected to show a different behavior with the crystals for each structure. However, we see that the spectrum from the structure with point defects and the structure with RDAs did not show a distinct difference from that of the crystalline one. The reason is that 0.24 at.% of point defects or RDAs in the middle region is not sufficient to be detected by the RBS/C measurements. We increase the concentration of defects to 0.5 at.% for point defects and RDAs. The RBS/C simulations from these two additional structures were performed, and the results are shown in Fig. 8. Here we can clearly see that the RBS/C yields from structures containing defects differ from the pristine crystals and these defects become detectable.

With the same fraction of defects, the RBS/C yields from the structure with RDAs in Fig. 8 are obviously lower than those from the structure with point defects. This result clearly shows that the defect model of RDAs, which is commonly used in RBS/C simulations, will overestimate the fraction of defective atoms, since the lattice distortion induced by the defective atoms is not taken into account. This conclusion is consistent with the one previously obtained from the the RBS/C simulation in silicon [19].

B. Dechanneling of probe ions

As is assumed in the standard analysis of RBS/C spectra (two-beam model), the RBS/C yields are formed due to the interactions of channeling ions with displaced (defective) atoms and the interactions of dechanneled ions with the rest

of the material atoms. The RBS/C yields $\chi_D(z)$ which are normalized by the yields from the amorphous structure can be expressed as [4]

$$\chi_D(z) = \chi_R(z) + [1 - \chi_R(z)]f n_D(z)/n, \tag{8}$$

where $\chi_R(z)$ is the fraction of the dechanneled ions, $n_D(z)$ is the concentration of the defective atoms, n is the crystal atomic density, and f is the defect scattering factor. The first term on the right-hand side, $\chi_R(z)$, describes the interactions of dechanneled ions with material atoms, and the second term describes the interactions of channeling ions with defective atoms.

The structures in the surface and deep bulk region are perfectly crystalline according to the depth profiles of defects expressed by Eq. (7), i.e., $n_D(z) = 0$. Then we have $\chi_R(z) = \chi_D(z)$, if we use $n_D(z) = 0$ in Eq. (8). This means the fraction of dechanneled ions in the surface or deep bulk region can be denoted by the normalized RBS/C yield. From Fig. 7, the fraction of dechanneled ions after getting through the middle region with extended defects is much larger than that after getting through the region with point defects. This indicates that, with the same amount of defective atoms, extended defects would lead to more probe ion dechanneling than either point defects or RDAs.

To study the dechanneling of probe ions, the concentration of defect RDAs in the middle region ($900 < z < 1800$) was increased to 20 at.%. With this concentration, the RBS/C signals showed a distinct difference from that from the perfect crystal, as shown in Fig. 9(a).

The fraction of dechanneled ions $\chi_R(z)$ while passing through the materials can be written as [7]

$$\chi_R(z) = \chi_v(z) + [1 - \chi_v(z)]\left[1 - \exp\left(-\int_0^z \sigma_D n_D(z')\,\mathrm{d}z'\right)\right], \tag{9}$$

where $\chi_v(z)$ is the RBS yield from the pristine crystals normalized by the yield from the amorphous structure, and σ_D is the dechanneling cross section (or dechanneling factor) for a given defect. This equation was used to fit the fraction of ions dechanneling in the surface and deep bulk region. The fraction of dechanneled ions in the middle region can be deduced by fitting the fractions of dechanneled ions in the surface and deep in the bulk. The deduced fraction of dechanneled ions $\chi_R(z)$ passing through the structures with RDAs and extended defects was shown by the black lines in Figs. 9(a) and 9(b), respectively.

Knowing the fraction of the dechanneled ions, $\chi_R(z)$, the RBS yield contributed by the interaction of channeling ions with defects (direct scattering) and by the interaction of dechanneled ions with atoms can be distinguished according to Eq. (8). As shown in Figs. 9(a) and 9(b), the yellow area denotes the RBS/C yields collected due to the increase of dechanneled ions, while the green area is the yield from direct backscattering from defective atoms. Comparison of the proportions of green (or yellow) areas in two figures allows us to determine the preferred mechanism of defects contributing in the final RBS/C spectra. For instance, in the spectra obtained from the structure with RDAs [Fig. 9(a)], the signals obtained from direct backscattering on RDAs were comparable with that obtained from the dechanneled ions; i.e., both of those mechanisms are of roughly equal significance.
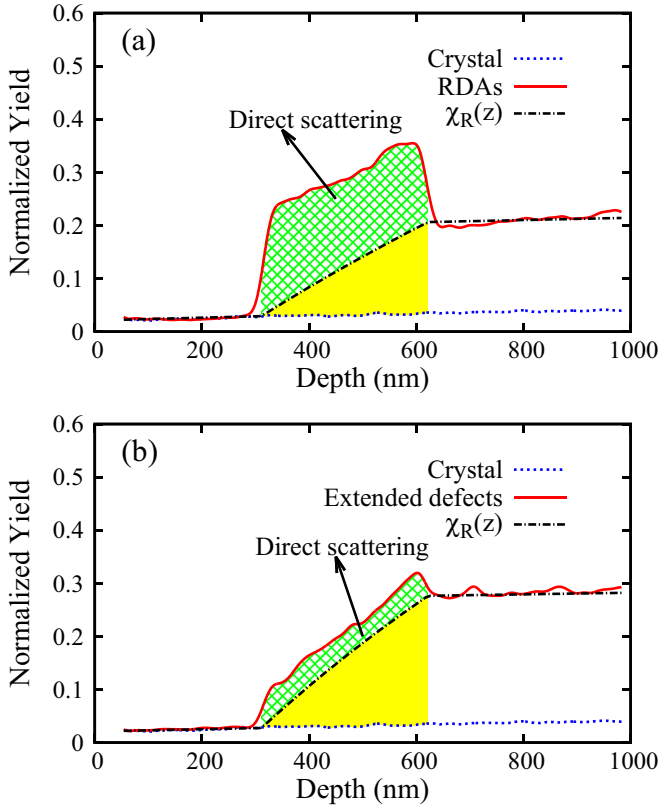
FIG. 9. (a) The RBS/C spectra (red line) from the structure with 20 at.% randomly displaced atoms. (b) RBS/C spectra (red line) from the structure with 0.24 at.% extended defects. In both (a) and (b), the RBS/C yield (Y axis) was normalized by the nonchanneling RBS yields; $\chi_R(z)$ (black line) denotes the fraction of dechanneled ions, and the blue line indicates the RBS/C signals from perfect crystalline structure.

However, the analysis of the spectra from the structure with extended defects [Fig. 9(b)] indicates that the contribution of direct scattering is insignificant, which means that the extended defects affect the RBS/C yield rather by increasing the fraction of the dechanneled ions. This conclusion is consistent with the previous study, in which the contribution of directing backscattering was approximately ignored in the analysis of RBS/C spectra from ion-implanted Al samples where extended defects were predominant [54].

C. Comparison with experiments

The experimentally obtained RBS/C spectrum from the Ni sample irradiated by 1.5 MeV Mn^+ ions with the fluence of $\Phi = 6.4 \times 10^{13}$ cm^{-2} is shown as green symbols in Fig. 10(a). The black and the symbols here demonstrate the RBS/C spectrum obtained experimentally from the random and the pristine crystal samples, respectively. The purple and orange lines are the simulated spectrum from random (amorphous) and crystalline structures, respectively.

To fit the experimental results, we created structures containing either RDAs or extended defects. We use the defect model of RDAs instead of Frenkel point defects here, since (i) RDAs have been widely used as the model defects for RBS/C
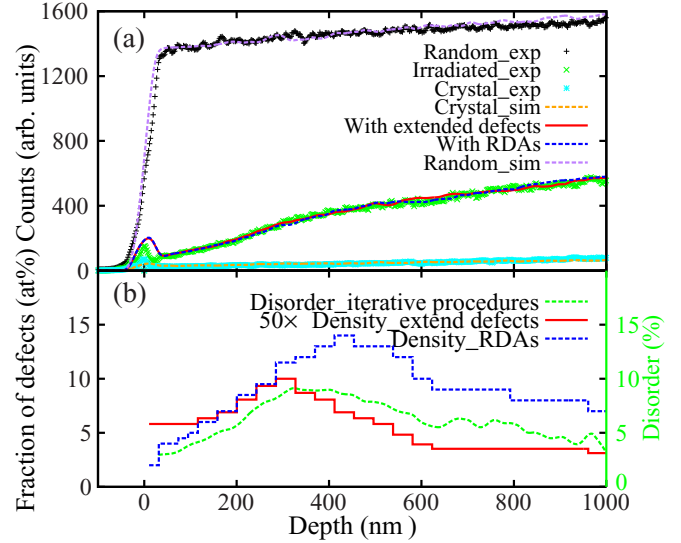

FIG. 10. (a) The comparison of the experimental (black, green, and cyan markers) and simulated (orange, red, blue, and purple lines) RBS/C spectra of Ni samples. The cyan (orange) and black (purple) show the spectra of pristine crystal and fully amorphous reference structures obtained by experiment (simulations). The green markers show the experimental result for a Ni sample irradiated by Mn^+ ions ($E_0 = 1.5$ MeV, $\Phi = 6.4 \times 10^{13}$ cm^{-2}). The blue and red lines are the fitted RBS/C spectra from the structure with RDAs and the structure with extended defects, respectively. (b) The depth profile of defects. The blue line is the depth profile (left y axis) of RDAs corresponding to the fitted RBS/C spectrum in (a), while the red line is the fitted depth profile (left y axis) of extended defects multiplied by 50. The green dashed line denotes the depth profiles (right y axis) of disorder extracted by the iterative procedure [5].

simulations and (ii) it is impossible to create the large fraction of noninteracting Frenkel point defects.

The experimental RBS/C spectrum from the irradiated sample was fitted by adjusting the depth profiles of the defects. The resulting fitted RBS/C spectrum from the structure with RDAs is shown in Fig. 10(a) by a blue line, while the fitted spectrum from the structure containing extended defects is shown by a red line. Both of these spectra show a very good agreement with the experimental results, except in the first few tens of nanometers region. The small discrepancy between the experimental and simulated RBS/C signals in this region can be attributed to the complex of surface structures in the experimental samples, e.g., relaxation and reconstruction of surface structures, maybe the existence of impurities, and other complex factors.

The blue dashed line in Fig. 10(b) demonstrates the depth profile of the RDAs corresponding to the fitted RBS/C spectra, while the red solid line is the profile of the densities of extended defects multiplied by 50. Here, the densities of these two kinds of defects are shown in terms of the fraction of defect atoms (left y axis), i.e., the ratio of defect atoms to total number of atoms in simulations. For extended defects, the defect atoms were counted by the number of added atoms (interstitials) forming the extrinsic SFs and removed atoms (vacancies) forming the SFT. The green dashed line in Fig. 10(b) denotes the depth profiles of the disorder (right y axis) extracted by the
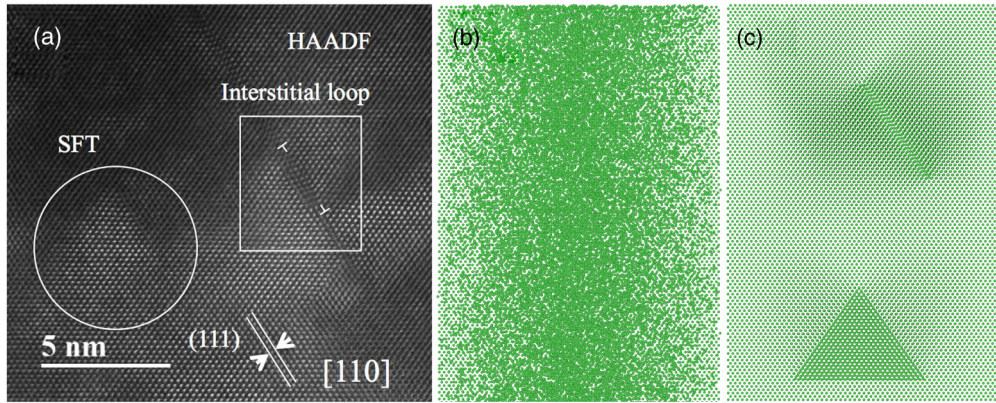
FIG. 11. (a) A high-resolution high angle annular dark field (HAADF) STEM image of irradiated Ni. Reproduced from Ref. [25]. (b) ⟨110⟩ view of a structure with 10 at.% RDAs. (c) ⟨110⟩ view of a structure with 0.2 at.% extended defects.

iterative procedure [5] method. Here the disorder, including all kinds of imperfection in crystals, is a comprehensive quantity that measures the damage in the irradiated sample.

In the irradiated sample used in the current work, the displacement per atom (dpa) in the region of the maximum of deposited energy in nuclear collisions is about 0.076 according to the NRT equation [55]. Usually, the dpa value is an overestimation of the amount of defects generated by ion irradiation in metals [56]. Experiments and MD simulations of collision cascades have shown that most of the displaced atoms in the initial collision stage will recover to a lattice position and only a few defects will remain finally [57–60]. The concentration of RDAs needed to fit the experimental results is up to 14 at.%. This is an obvious overestimation of defect concentration even compared to the dpa values, although the latter is already an overestimation itself compared to the number of realistically created defects in the irradiated sample. Moreover, the high-resolution scanning transmission electron microscopy (STEM) image [Fig. 11(a)] of Ni after irradiation was measured in Ref. [25]. The comparison of an atom structure containing 10 at.% RDAs [Fig. 11(b)] and the STEM image [Fig. 11(a)] of irradiated Ni showed clearly that the concentration of defects should be far smaller than 10 at.%. Therefore, we concluded that using the RDAs to imitate the defects in the irradiated Ni sample would lead to overestimating the concentration of defects.

The previous collision cascade simulation in Ni showed that only less than 1 at.% defects were observed after Ni samples were irradiated up to about 0.5 dpa [61]. Besides, the diffuse x-ray scattering measurement in Ni irradiated by self-ions to 1 dpa also shows that less than 1 at.% of defects were observed [62]. Furthermore, as shown in the STEM image [Fig. 11(a)], most of the atoms were still in the lattice position and only a small fraction of defective atoms were observed after irradiation. However, such strong RBS/C signals as those from the structure with more than 10 at.% RDAs were observed in the experiment, even though both the experiments and MD simulation showed only a small fraction of displaced atoms. The current RBS/C simulation from the structure with extended defects reveals the reason for this phenomenon. The key observation is that a small fraction (about 0.2 at.%) of extended defects leads to a RBS/C spectrum that is similar to the one generated by the structure with more than 10

at.% RDAs. The ⟨110⟩ view of a structure with 0.2 at.% of extended defects is shown in Fig. 11(c). Comparison of this structure and the STEM image shows the structure with extended defects is more reasonable than that with RDAs. Therefore, the agglomeration of defects created by irradiation which leads to the formation of extended defects enhances the probability of probe ion dechanneling, which is reflected in the RBS/C spectra of ion-irradiated Ni as signals from a heavily damaged sample, while such heavy damage is not observed by experiment or collision cascade simulation.

In Fig. 10(b), not only are the concentrations of defects completely different, but also the depth profiles of the RDAs and the extended defects show a visible discrepancy. As we can see, the damage peaks fitted by assuming RDAs are deeper than that fitted by assuming extended defects. This discrepancy arises from the different mechanisms of how the defects affect the RBS/C signals (see Fig. 9). The normalized depth profile of extended defects is consistent with the depth of the disorder obtained by the iterative procedure, which is another proof that the disorder in irradiated Ni extracted by RBS/C is mainly from a small fraction of extended defects, rather than the RDAs.

V. CONCLUSIONS

In conclusion, we developed a BCA code to simulate the RBS/C spectra from arbitrary atomic structures described by a set of atomic coordinates (which can, e.g., be obtained from an independent MD simulation). We used the MD method to create the atomic structures of Ni samples with different types of defects, namely, randomly displaced atoms, point defects, and extended defects. The comparison and analysis of simulation results reveal that (a) the commonly used model of defects in RBS/C simulations, randomly displaced atoms, leads to strong overestimation of number of defects in Ni, since the lattice distortion induced by the defective atoms is not taken into account; (b) the RBS/C signal is more sensitive to the extended defects than to point defects, and the strong long-range strain field induced by extended defects is suggested to explain this difference; and (c) instead of by directly leading to probe ions backscattering, the extended defect increases the RBS/C yields by increasing the dechanneling probability of channeling probe ions. Finally, we compared the simulation results with the experiment. Through the comparison, we

[1] Y. Zhang, M. Ishimaru, J. Jagielski, W. Zhang, Z. Zhu, L. V. Saraf, W. Jiang, L. Thome, and W. J. Weber, J. Phys. D: Appl. Phys. **43**, 085303 (2010).

[2] G. Lulli, M. Bianconi, A. Parisini, S. Sama, and M. Servidori, J. Appl. Phys. **88**, 3993 (2000).

[3] L. Zhang, R. Fadanelli, P. Hu, J. Zhao, T. Wang, and C. Zhang, Nucl. Instrum. Methods Phys. Res., Sect. B **356-357**, 53 (2015).

[4] E. Błogh, Can. J. Phys. **46**(6), 653 (1968).

[5] Y. Zhang, J. Lian, Z. Zhu, W. Bennett, L. Saraf, J. Rausch, C. Hendricks, R. Ewing, and W. Weber, J. Nucl. Mater. **389**, 303 (2009).

[6] L. Shao and M. Nastasi, Appl. Phys. Lett. **87**, 064103 (2005).

[7] L. C. Feldman, J. W. Mayer, and S. T. Picraux, *Materials Analysis by Ion Channeling: Submicron Crystallography* (Academic Press, New York, 1982).

[8] J. A. Leavitt, L. C. McIntyre, Jr., and M. R. Weller, in *Handbook of Modern Ion Beam Analysis*, edited by J. R. Tesmer and M. Nastasi (Materials Reseach Society, Pittsburgh, PA, 1995).

[9] J. Williams and R. Elliman, in *Ion Beams for Materials Analysis*, edited by J. Bird and J. Williams (Academic Press, Sydney, 1989).

[10] J. H. Barrett, Phys. Rev. B **3**, 1527 (1971).

[11] P. J. M. Smulders and D. O. Boerma, Nucl. Instrum. Methods Phys. Res. **29**, 471 (1987).

[12] L. Nowicki, A. Turos, R. Ratajczak, A. Stonert, and F. Garrido, Nucl. Instrum. Methods Phys. Res., Sect. B **240**, 277 (2005).

[13] E. Albertazzi, M. Bianconi, G. Lulli, R. Nipoti, and M. Cantiano, Nucl. Instrum. Methods Phys. Res., Sect. B **118**, 128 (1996).

[14] G. Lulli, E. Albertazzi, M. Bianconi, G. Bentini, R. Nipoti, and R. Lotti, Nucl. Instrum. Methods Phys. Res., Sect. B **170**, 1 (2000).

[15] J. Jagielski, L. Thom, Y. Zhang, C. Wang, A. Turos, L. Nowicki, K. Pagowska, and I. Jozwik, Nucl. Instrum. Methods Phys. Res., Sect. B **268**, 2056 (2010).

[16] A. Turos, P. Jozwik, L. Nowicki, and N. Sathish, Nucl. Instrum. Methods Phys. Res., Sect. B **332**, 50 (2014).

[17] M. T. Robinson and I. M. Torrens, Phys. Rev. B **9**, 5008 (1974).

[18] S. Balboni, E. Albertazzi, M. Bianconi, and G. Lulli, Phys. Rev. B **66**, 045202 (2002).

[19] G. Lulli, E. Albertazzi, M. Bianconi, A. Satta, S. Balboni, and L. Colombo, Phys. Rev. B **69**, 165216 (2004).

[20] Y. Zhang, M. Crespillo, H. Xue, K. Jin, C. Chen, C. Fontana, J. Graham, and W. Weber, Nucl. Instrum. Methods Phys. Res., Sect. B **338**, 19 (2014).

[21] T. Wang, J. Zhao, M. Lan, Q. He, K. Fang, X. Guan, and X. Xu, Nucl. Instrum. Methods Phys. Res., Sect. B **269**, 2721 (2011).

[22] J. P. Biersack and L. G. Haggmark, Nucl. Instrum. Methods **174**, 257 (1980).

[23] J. F. Ziegler, SRIM-2008.04 software package, http://www.srim.org.

[24] M. Posselt and J. Biersack, Nucl. Instrum. Methods Phys. Res., Sect. B **64**, 706 (1992).

[25] C. Lu, K. Jin, L. K. Béland, F. Zhang, T. Yang, L. Qiao, Y. Zhang, H. Bei, H. M. Christen, R. E. Stoller, and L. Wang, Sci. Rep. **6**, 19994 (2016).

[26] D. S. Aidhy, C. Lu, K. Jin, H. Bei, Y. Zhang, L. Wang, and W. J. Weber, Acta Mater. **99**, 69 (2015).

[27] Y. Zhang, G. M. Stocks, K. Jin, C. Lu, H. Bei, B. C. Sales, L. Wang, L. K. Beland, R. E. Stoller, G. D. Samolyuk, M. Caro, A. Caro, and W. J. Weber, Nat. Commun. **6**, 19994 (2015).

[28] F. G. Djurabekova, T. S. Pugacheva, F. F. Umarov, and S. V. Yugay, in *Proceedings of the 13th Ion Implantation Technology–International Conference* (IEEE, New York, 2000), pp. 228–231.

[29] M. P. Allen and D. J. Tildesley, *Computer Simulation of Liquids* (Oxford University Press, Oxford, UK, 1989).

[30] K. Nordlund, 2010, PARCAS computer code. The main principles of the molecular dynamics algorithms are presented in Ref. [60]. The adaptive time step and electronic stopping algorithms are the same as in Ref. [34].

[31] M. Ghaly, K. Nordlund, and R. S. Averback, Philos. Mag. A **79**, 795 (1999).

[32] J. Ziegler, J. Biersack, and U. Littmark, *The Stopping and Range of Ions in Matter* (Pergamon, New York, 1985).

[33] B. Yuan, P. Yu, and S. Tang, Nucl. Instrum. Methods Phys. Res., Sect. B **83**, 413 (1993).

[34] K. Nordlund, Comput. Mater. Sci. **3**, 448 (1995).

[35] K. Nordlund, J. Keinonen, E. Rauhala, and T. Ahlgren, Phys. Rev. B **52**, 15170 (1995).

[36] P. Haussalo, K. Nordlund, and J. Keinonen, Nucl. Instrum. Methods Phys. Res., Sect. B **111**, 1 (1996).

[37] J. Sillanpää, K. Nordlund, and J. Keinonen, Phys. Rev. B **62**, 3109 (2000).

[38] J. Sillanpää, J. Peltola, K. Nordlund, J. Keinonen, and M. J. Puska, Phys. Rev. B **63**, 134113 (2001).

[39] J. Sillanpää, Nucl. Instrum. Methods Phys. Res., Sect. B **164**, 302 (2000).

[40] J. Peltola, K. Nordlund, and J. Keinonen, Nucl. Instrum. Methods Phys. Res., Sect. B **212**, 118 (2003).

[41] H. Y. Chan, K. Nordlund, J. Peltola, H.-J. Gossmann, N. L. Ma, M. P. Srinivasan, F. Benistant, and L. Chan, Nucl. Instrum. Methods Phys. Res., Sect. B **228**, 240 (2005).

[42] C. Kittel, *Introduction to Solid State Physics* (Wiley, Hoboken, NJ, 2005).

[43] K. Arstila, T. Sajavaara, and J. Keinonen, Nucl. Instrum. Methods Phys. Res., Sect. B **174**, 163 (2001).

[44] A. V. Krasheninnikov and K. Nordlund, J. Appl. Phys. **107**, 071301 (2010).

[45] K. Nordlund and F. Djurabekova, J. Comput. Electr. **13**, 122 (2014).

[46] S. Plimpton, J. Comput. Phys. **117**, 1 (1995).

[47] X. W. Zhou, R. A. Johnson, and H. N. G. Wadley, Phys. Rev. B **69**, 144113 (2004).

[48] J. Silcox and P. B. Hirsch, Philos. Mag. **4**, 72 (1959).

[49] M. de Jong and J. S. Koehler, Phys. Rev. **129**, 49 (1963).

[50] B. P. Uberuaga, R. G. Hoagland, A. F. Voter, and S. M. Valone, Phys. Rev. Lett. **99**, 135501 (2007).

[51] B. Wirth, V. Bulatov, and T. D. de la Rubia, J. Nucl. Mater. **283–287**, 773 (2000).

[52] D. S. Aidhy, C. Lu, K. Jin, H. Bei, Y. Zhang, L. Wang, and W. J. Weber, Scr. Mater. **114**, 137 (2016).

[53] A. Stukowski, Modell. Simul. Mater. Sci. Eng. **18**, 015012 (2010).

[54] S. T. Picraux, D. M. Follstaedt, P. Baeri, S. U. Campisano, G. Foti, and E. Rimini, Radiat. Eff. **49**, 75 (1980).

[55] M. J. Norgett, M. T. Robinson, and I. M. Torrens, Nucl. Eng. Des. **33**, 50 (1975).

[56] K. Nordlund, S. J. Zinkle, T. Suzudo, R. S. Averback, A. Meinander, F. Granberg, L. Malerba, R. Stoller, F. Banhart, B. Weber, F. Willaime, S. Dudarev, and D. Simeone, *Primary Radiation Damage in Materials: Review of Current Understanding and Proposed New Standard Displacement Damage Model to Incorporate In-Cascade Mixing and Defect Production Efficiency Effects* (OECD Nuclear Energy Agency, Paris, 2015).

[57] R. S. Averback, R. Benedek, and K. L. Merkle, Phys. Rev. B **18**, 4156 (1978).

[58] R. S. Averback and T. Diaz de la Rubia, in *Solid State Physics*, edited by H. Ehrenfest and F. Spaepen (Academic Press, New York, 1998), Vol. 51, pp. 281–402.

[59] T. Diaz de la Rubia, R. S. Averback, R. Benedek, and W. E. King, Phys. Rev. Lett. **59**, 1930 (1987); see also **60**, 76(E) (1988).

[60] K. Nordlund, M. Ghaly, R. S. Averback, M. Caturla, T. Diaz de la Rubia, and J. Tarus, Phys. Rev. B **57**, 7556 (1998).

[61] F. Granberg, K. Nordlund, M. W. Ullah, K. Jin, C. Lu, H. Bei, L. M. Wang, F. Djurabekova, W. J. Weber, and Y. Zhang, Phys. Rev. Lett. **116**, 135504 (2016).

[62] R. J. Olsen, K. Jin, C. Lu, L. K. Beland, L. Wang, H. Bei, E. D. Specht, and B. C. Larson, J. Nucl. Mater. **469**, 153 (2016).